RSC Advances

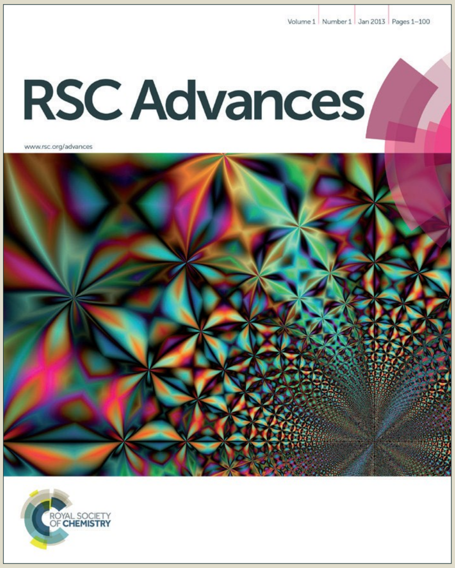

ROYAL SOCIETY OF CHEMISTRY

www.rsc.org/advances

Using Maximum Entropy Approach for Prediction of Drop Size Distribution in a Pilot Plant Multi-Impeller Extraction Contactor

Mehdi Asadollahzadeh[a,b], Meisam Torab-Mostaedi[b]*, Shahrokh Shahhosseini[a], Ahad Ghaemi[a]

[a] Department of Chemical Engineering, Iran University of Science and Technology (IUST), P.O. Box 16765-163, Tehran, Iran

[b] Nuclear Fuel Cycle Research School, Nuclear Science and Technology Research Institute, P.O. Box 11365-8486, Tehran, Iran

---

*Corresponding author: M. Torab-Mostaedi (mmostaedi@aeoi.org.ir)
Tel: +982188221117; Fax:+982188221116

Abstract

In this study, the maximum entropy principle is used to predict the drop size distributions in a multi-impeller column extractor. Three systems including toluene-water, n-butyl acetate-water and n-butanol-water were experienced in this column. An experimental study of mass transfer conditions was performed in which acetone was transferred between the organic and aqueous phases. The drop size distribution and Sauter mean drop diameter were found to depend largely on the rotor speed and interfacial tension, but, only partially dependent on the phase velocities. The empirical correlations are proposed to describe Lagrange multipliers in maximum entropy function in terms of operating variables and physical properties of the systems. In addition, an empirical correlation is proposed for estimation of the Sauter mean drop diameter. Also, the combination of computational fluid dynamics (CFD) and droplet population balance modeling (PBM) has been carried out to predict the drop size distributions. The comparison shows good agreement between the present models and the experimental data. Experimental results show that the maximum entropy function satisfies the droplet size distributions for three systems in a multi-impeller column extractor. The acquired information would be useful in design of liquid-liquid extraction columns.

Keywords: Maximum Entropy Method, Multi-Impeller Column Extractor, Drop Size Distribution, Sauter Mean Drop Diameter, Population Balance Equation.

1. Introduction

Many industrial processes such as solvent extraction and emulsification involve liquid–liquid dispersions in stirred vessels. The knowledge of the evolution of drop size distribution with changes of external mechanical energy input is of major importance in solvent extraction systems. In solvent extraction processes, the interfacial area of the dispersion controls the mass transfer rate and is a major parameter for the design and scaling-up of gravity settlers that warrant the ultimate liquid phases separation [1, 2].

Multi-impeller column extractors have been widely used in the chemical processes such as solvent extraction. The unit is neither a compartmental or truly continuously differential device, but has some properties of both. The motion of droplets between compartments in these columns is therefore dependent upon the droplet size, the physical properties of the phases, the phase flow rates and the agitator speed [3, 4]. The power input to the multi-impeller column extractors is thus transferred to the kinetic, surface, potential and heat energy of the droplets. The same mean drop size can be obtained from various drop size distributions which have different interfacial areas. Therefore, the change in mean drop size and drop size distribution with agitation speed is very important in these extractors [5, 6]. The unified correlations for prediction of the drop size in mechanically agitated columns are shown in Table 1.

The effects of agitation speed and mass transfer on the Sauter mean drop diameter in the multi-impeller column extractor were investigated by Komasawa and Ingham, 1978 [7]. The Suater mean drop diameter decreases as the rotor speed increases up to a certain agitation level, above which drop breakage and coalescence become equally important and the Suater mean drop diameter remains unchanged.

Tsouris et al., 1990 [8] studied the experiments in multi-impeller column extractor and it was observed that drop size distributions were broad in the first stages of the column, becoming narrower and smaller drop sizes along the column.

Several empirical correlations have been proposed to characterize the distribution of droplet sizes in liquid-liquid extraction columns, normal [9, 10], log-normal [5, 11], Weibull [12] and Gamma[13] functions.

As an alternative to the empirical approach, analytical approaches to address the problem of modeling droplet size distribution have been developed in the past two decades. There are two different approaches to deal with the hydrodynamics and mass transfer in liquid-liquid extraction columns, i.e. the drop population balance model (DPBM) [14-16] and the computational fluid dynamics (CFD) [17-20].

The application of the DPBM implies the knowledge of an appropriated model for breakage and coalescence of drops, besides the usual parameters such as holdup, drops diameter and mass transfer coefficients. Later on, a complex mathematical model is applied for solving the equations. The dynamic behavior of particulate processes under the influence of the nonlinear aggregation term, nucleation, growth and breakup was studied by population balance equation [21]. Simulation of aromatics extraction with population balance model in a pilot-plant Kühni extractor investigated by Buchbender and co-workers [22].

Computational fluid dynamics has emerged as a potential tool for liquid-liquid extraction studies. It involves the solution of the conservation equations of momentum, mass and volume fractions for different phases at a number of grid points in the column[18].The sufficient resolution for capturing the different aspects of the flows needs for complex hydrodynamics in these columns. Therefore, it leads to requirements of large computational power in terms of capacity and storage.

Other methods for prediction of drop size distribution are maximum entropy method and probability distribution function. The maximum entropy approach is a method of statistical inference that provides the least biased estimate of a probability distribution, consistent with a set of constraints that express the available information about the relevant phenomena [23, 24].

There are a few literature data on the study of the multi-impeller column extractors investigating the drop size and drop size distribution, experimentally. In addition, a statistical approach has not been attempted to derive the most probable drop size distribution in these columns.

In this article, we investigated measurements drop size distribution and mean drop diameter across a multi-impeller column extractor and compared these results with predictions obtained using the maximum entropy principle. In the process of making these comparisons, estimates will be made of the constant parameters in the maximum entropy approach as a function of effective variables. In addition, a combination of computational fluid dynamics (CFD) and droplet population balance modeling (PBM) is applied to simulate the drop size distributions. The results from the simulation are compared with the results obtained from maximum entropy approach.

2. Maximum entropy approach

Maximum entropy is a popular technique that is utilized to construct the probability distribution functions of stochastic fields where limited information is available. There are often limitations on the amount of information available due to the high costs involved in performing a great number of experiments or simulations. The concept of information entropy was developed by Shannon, 1948 [25] and Jaynes, 1957 [26]. The principle of this approach in thermodynamics investigated by Tribus and Princeton [27]. They showed that the concepts of heat and temperature in thermodynamics could be defined through the formalism of maximum entropy.

Sobrino et al., 2009 [28] investigated into maximum entropy approach for the determination of bubble size distribution in fluidized bed. The maximum entropy approach has been shown to be a simple procedure that offers many benefits over other procedures applied before for size distribution modeling in fluidized beds.

Droplet size and velocity distributions for spray modeling were reported by Jones and Watkins, 2012 [29]. Results showed that the maximum entropy function combined with the gamma distribution assure these conditions for the droplet size distributions in spray modeling. The grain size distributions of polycrystalline materials cannot easily be measured experimentally since they vary even at a specific point for different samples of the material. Sankaran and Zabaras, 2007 used the maximum entropy principle to compute a probability distribution functions of microstructures based on given information about a microstructural system [30].

The idea of entropy (information uncertainty) of a probability distribution was introduced by Shannon, 1948 [25], who showed that for the different states of material, each of them having the probability (P_i) and the uncertainty of the probability distribution is given by

$$S(P_i) = -k\sum_{i=1}^{n} P_i \ln P_i \tag{7}$$

where k is a constant parameter and n is number of states of material. Because of its similarity to the thermodynamic entropy (S) is named Shannon's entropy. The limitations mathematically express the mean values of information accessible. If $f_k(D)$ is a function describing a droplet property such as mass or momentum and its known mean value over all droplets is F_k, the corresponding constraint written for all the size classes is:

$$\sum_{i=1}^{n} P_i f_k(D_i) = F_k \tag{8}$$

In the case of mass conservation ($f_k\ (D_i) = m_i$), the mass m before droplet breakage in the column must be equal to the sum of all droplet masses after droplet breakage:

$$m = \sum_{i=1}^{n} m_i = \frac{\pi}{6}\rho_l N \sum_{i=1}^{n} D_i^3 P_i \tag{9}$$

In Eq.9, n is the number of drop size classes, D_i is the arithmetic mean diameter of the drops in size class i, N is the total number of drops within the control volume and P_i is the probability parameter that a droplet is in the size class i. The definition of relevant parameters is shown in Fig.1. The inclusion of the mean drop diameter d_{30} via the relation $m = \frac{\pi}{6}\rho_l N d_{30}^3$ finally results in the mass conservation constraint for maximum entropy function:

$$\sum_{i=1}^{n} \frac{D_i^3}{d_{30}^3} P_i = 1 \tag{10}$$

Another constraint arises from the normalization of the set of probabilities:

$$\sum_{i=1}^{n} P_i = 1 \tag{11}$$

By using Lagrange multipliers (λ), the probability distribution function is defined as:

$$P_i = exp\left[-\lambda_0 - \sum_{r=1}^{m} \lambda_r f_r(d_i) \right] \tag{12}$$

where r is a counter, m is the number of constrains; and $f_r\ (d_i)$ is average value.

By using constraints in equations 10 and 11, the relationship between Lagrange multipliers is obtained as follows:

$$exp(\lambda_0) = \sum_{k} exp\left[-\sum_{r=1}^{m} \lambda_r f_r(d_i) \right] \tag{13}$$

$$F_k\ exp(\lambda_0) = \sum_{k} exp\left[-\sum_{r=1}^{m} \lambda_r f_r(d_i) \right] \tag{14}$$

The above equations in continuous space for drop size distribution are rewritten as follows:

$$S = -k\int_0^\infty P\,ln(P)d(d) \tag{15}$$

$$\int_0^\infty P f_k d(d) = F_k \tag{16}$$

$$\int_0^\infty P_n(d)d(d) = 1 \tag{17}$$

$$\int_0^\infty P_n(d)d^3 d(d) = d_{30}^3 \tag{18}$$

$$\int_0^\infty P_n(d)d^2 d(d) = \frac{d_{30}^3}{d_{32}} \tag{19}$$

The problem of finding the most likely size distribution is expressed mathematically by a maximization problem. The maximum of the function defined in Eq. (15) has to be calculated subject to the constraints. The general result of the application of the above equations to a particular problem is:

$$P_i = exp(-\lambda_0 - \lambda_1 f_1^{\,2}(d_i) - \lambda_2 f_2^{\,3}(d_i)) \tag{20}$$

where the set of λ is a collection of Lagrange multipliers which must be evaluated for each particular solution. The constraints (Eqs. 16 to 19) are used for to evaluate the Lagrange multipliers, which results in a system of non-linear equations that have to be solved.

3. Numerical approach

A combination of computational fluid dynamics (CFD) and droplet population balance modeling (PBM) is applied to simulate the drop size distributions. The CFD equation can predict the energy dissipation, volume fraction and velocity, while the PBM can account for the droplet coalescence and breakup and predict the size distribution of the dispersed phase. The finite-difference numerical method was used for solving the combination of CFD and PBM equations with Matlab software that the schematic of this procedure is shown in Fig. 2.

3.1. Eulerian- Eulerian model

An Euler-Euler model where both phases are treated mathematically as interpenetrating continua was applied for the two-phase simulations of the extraction column. The continuity and conservation of momentum equations for the continuous phase are:

$$\frac{\partial(\alpha_c\rho_c)}{\partial t}+\nabla.\left(\alpha_c\rho_c\overrightarrow{u_c}\right)=0 \tag{21}$$

$$\frac{\partial\left(\alpha_c\rho_c\overrightarrow{u_c}\right)}{\partial t}+\nabla.\left(\alpha_c\rho_c\overrightarrow{u_c}\overrightarrow{u_c}\right)-\nabla.\tau_c=-\alpha_c\nabla p+\alpha_c\rho_c g+F_{in} \tag{22}$$

where α, ρ, u, τ, p, g and F_{in} represent the volume fraction, phase density, phase velocity, stress- strain tensor, pressure, gravitational acceleration and the interfacial force, respectively. In addition to equation 1 and 2, the constraint for the volume fraction must be satisfied:

$$\alpha_1+\alpha_2=1 \tag{23}$$

The interphase interaction term F_{in} consists of different momentum exchange mechanisms. The drag force is calculated as follow:

$$F_{c,d}=\frac{3\rho_d\alpha_c\alpha_d C_d\left|\overrightarrow{u_d}-\overrightarrow{u_c}\right|\left(\overrightarrow{u_d}-\overrightarrow{u_c}\right)}{4d_d} \tag{24}$$

where the drag coefficient C_d was described by the model of Schiller-Naumann in simulation [31].

3.2. Turbulence k-ε model

A standard k-ε model is used to capture the effect of turbulence of continuous phase. The kinetic energy (k) and energy dissipation (ε) are described for continuous phase by the following equations:

$$\frac{\partial(\alpha_c\rho_c k_c)}{\partial t}+\nabla.\left(\alpha_c\rho_c k_c\overrightarrow{u_c}\right)=\nabla.\left(\alpha_c\frac{\mu_{t,c}}{\sigma_k}\nabla k_c\right)+\alpha_c G_{k,c}-\alpha_c\rho_c g+\alpha_c\rho_c\prod\nolimits_{k,c} \tag{25}$$

$$\frac{\partial(\alpha_c\rho_c\varepsilon_c)}{\partial t}+\nabla.\left(\alpha_c\rho_c\varepsilon_c\overrightarrow{u_c}\right)=\nabla.\left(\alpha_c\frac{\mu_{t,c}}{\sigma_k}\nabla\varepsilon_c\right)+\alpha_c\frac{\varepsilon_c}{k_c}\left(C_{1\varepsilon}G_{k,c}-C_{2\varepsilon}\rho_c\varepsilon_c\right)+\alpha_c\rho_c\prod\nolimits_{\varepsilon,c} \tag{26}$$

Where, $G_{k,c}$ represents the generation of turbulence kinetic energy because mean velocity gradients, $\Pi_{k,c}$ and $\Pi_{\varepsilon,c}$ represent the influence of the dispersed phase on the continuous phase and the values for C_1, C_2, C_μ, σ_k and σ_ε were reported by Kerdouss and co-workers [32].

3.3. Population balance model

The drop population balance model is based on the definition of a number density function *n(x,V,t)* representative of the volume distribution of drop sizes at a level x in the column.

The unsteady state drop population balance is given by the following equation:

$$\frac{\partial}{\partial t}\left[n(V,t)\right]+\nabla.\left[\vec{u}n(V,t)\right]=P(V,t) \tag{27}$$

where *P(V, t)* takes explicitly into account the influence of breakage and coalescence process. For each former mechanism, one can define respectively two functions *PB(V, t)* and *PC(V, t)* that can be divided into generation and sink terms for a drop class d, so that:

$$P(V,t)=PB^{+}(V,t)-PB^{-}(V,t)+PC^{+}(V,t)-PC^{-}(V,t) \tag{28}$$

In the latter expression, $PB^{+}(V, t)$ indicates of which are larger than d, and $PB^{-}(V, t)$ indicates the output term due to breakage of drops of class d. $PC^{+}(V, t)$ represents the input term due to coalescence of drops, the diameters of which are smaller than d, and $PC^{-}(V, t)$ represents the output term due to the coalescence of drops of class d with any other drop. The graphical representation of *PB(V, t)* and *PC(V, t)* in population balance equation is shown in Fig. 3 and the birth and death rates are given by

$$PB^{+}(V,t)=\int_{V}^{\infty}g_b\left(V'\right)\beta(V\,|\,V')n(V',t)dV' \tag{29}$$

$$PB^{-}(V,t)=g_b(V)n(V,t) \tag{30}$$

$$PC^{+}(V,t)=\frac{1}{2}\int_{0}^{V}a\left(V-V',V'\right)n(V-V',t)n(V',t)dV' \tag{31}$$

$$PC^{-}(V,t)=\int_{0}^{\infty}a\left(V,V'\right)n(V,t)n(V',t)dV' \tag{32}$$

The breakage rate expression in Eq. 29 includes the probability density function β, which describes the distribution of the daughter droplets from the splitting mother particle V' and the breakage frequency g_b.

The aggregation kernel a in the Eqs. 31and 32 accounts for the probability of successful collisions between pairs of droplets. It is defined as the product of the collision frequency h and the coalescence efficiency δ:

$$a(V,V') = h(V,V')\delta(V,V') \tag{33}$$

The breakage and coalescence in the dispersed phase was described by Coulaloglou and Tavlarides hydrodynamic model [33]. The coalescence term uses the frequently applied structure of the product of drop–drop collision frequency and coalescence efficiency. This model is given by the following set of equations:

$$g_b(d) = C_1 \frac{\varepsilon^{1/3}}{d^{2/3}(1+\alpha)} exp(-\frac{C_2\sigma(1+\alpha)^2}{\rho_d \varepsilon^{2/3} d^{5/3}}) \tag{34}$$

$$h(d_1,d_2) = C_3 \frac{\varepsilon^{1/3}}{(1+\alpha)} (d_1+d_2)^2 \left(d_1^{2/3}+d_2^{2/3}\right)^{1/2} \tag{35}$$

$$\delta(d_1,d_2) = exp(-C_4 \frac{\mu_c \rho_c \varepsilon}{\sigma^2(1+\alpha)^3} \left(\frac{d_1 d_2}{d_1+d_2}\right)^4) \tag{36}$$

Where C_1, C_2, C_3 and C_4 are adjustable parameters in the above equations. The originally used normal density function for the daughter droplet distribution of Valentas and co-workers [34], which assumes binary breakage, is also adopted here:

$$\beta\left(d_1^3 \middle| d_2^3\right) = \frac{2.4}{d_2^3} exp(-\frac{4.5\left(2d_1^3 - d_2^3\right)^2}{d_2^6}) \tag{37}$$

4. Experimental

4.1. Chemical Systems

Three various systems with different interfacial tensions consisting of toluene–water (high interfacial tension), n-butyl acetate–water (medium interfacial tension) and n-butanol-water (low interfacial tension) were used for experiments without mass transfer. Two systems involving toluene-acetone-water and n-butyl acetate–acetone-water were used for experiments with two direction of mass transfer. The European Federation of Chemical Engineering (E.F.C.E) has adopted these systems as official test systems for investigation of extraction [35]. The physical properties for the three systems are shown in Table 2. Purity of organic phase solvents are more than 99.5% and all solvents are used without purification. In experiments with mass transfer, dilute solutions were investigated with approximately 3.5 wt% acetone as transferred solute in the organic or aqueous phase.

4.2. Multi-impeller column extractor experiments

The schematic flow diagram of the multi-impeller column extractor is shown in Fig.4. The column was made of a cylindrical glass section and was equipped with impellers with accurate speed control, whereas the internal parts were constructed of stainless steel. The main section was made of Pyrex glass, 113 mm I.D, and the height of the column with nine stages was 700 mm. The nine stages were formed by rings of 25% free area as compared with the column cross-sectional area. Mixing was done by nine 6-blade impellers of 50 mm diameter located at the center of each stage and these impellers were driven by an electric motor via a variable gearbox.

The organic phase (dispersed phase) and water (continuous phase) were fed into the extraction column at the bottom and on the top respectively in counter-current mode. Two flow meters were employed to supply and monitor the fixed flow rates of the continuous and dispersed phases. The inlet and outlet of the column were connected to four tanks with each of 85 L capacity. The interface was maintained at the required level by means of an optical sensor as previously described [36].

When the operation became steady state condition, the inlet and outlet valves were quickly closed. The dispersed phase was allowed to settle and the difference in the interface level location was used to measure the total holdup. Acetone concentrations of input and output streams of the column for continuous and dispersed phases were analyzed by UV-visible spectroscopy.

4.3. Drop size measurement

The drop size was measured by means of a very high-resolution Nikon D5000 digital camera used to take a digital photo of extractor contents. Next, droplet dimensions were compared with the thickness of stators as a reference size in these pictures. The four different heights of active column were selected to determine the size of droplets.

The curved surface of the glass extraction column and significant differences between air and the glass refractive indices were found to lead to a parallax deformation of the objects photographed in the column extractor. In order to exclude this phenomenon, a container filled with water was attached to the extraction contactor and the photographic approach was adopted to calculate the size of the stator thickness served as the reference for measurements of drop size. Consequently, digital image analysis software was applied in order to investigate the taken high quality photograph. Finally, a minimum of 1000 drops was analyzed for each experimental picture in order to guarantee the statistical significance of the determined size distributions. The Sauter mean diameter was calculated from the following equation:

$$d_{32} = \frac{\sum_{i=1}^{N} n_i d_i^3}{\sum_{i=1}^{N} n_i d_i^2} \tag{38}$$

where n_i denotes the number of drops of diameter d_i.

5. Results and discussion

5.1. Mean drop size

The experimental results for Sauter mean drop size with agitation speed are shown in Fig.5. The significant result to observe is that Sauter mean drop diameters decrease with an increase in agitation speed. The explanation for this effect is related to the increment in the frequency of drop collisions against the internal parts of the column extractor in more turbulent fluid flow in their ascending path inside the equipment.

The effects of the dispersed and continuous phase velocities on the mean drop diameter were tested, which are illustrated in Fig. 6 and 7. The mean drop diameter increased with an increase in dispersed phase velocity, while a slight increase occurred at low interfacial tension. This observation relates to the increasing drop collisions with the acceleration of the dispersed phase velocity and consequently the coalescence frequency among the drops is increased. According to Fig.7, the variations in the mean drop diameter with increasing continuous phase velocity are insignificant.

To supplement the investigation into the effect of operating parameters used in this study, three systems were adopted to check the effect of the system properties (interfacial tension) on the mean drop diameters. The pictures of drop sizes for the three systems are shown in Fig 8.

From the results presented in Figs. 5 to 8, it was observed that smaller drops were generated from the low interfacial system (n-butanol-water) rather than from the medium or higher interfacial system (n-butyl acetate-water or toluene-water).

When there is no agitation, ratio of buoyancy to interfacial tension forces is responsible for the breakup of the drops and formation of the smaller drops. Thus, the drop size can be predicted by the following equation:

$$d_{32} = C\left(\frac{\sigma}{\Delta\rho g}\right)^{0.5} \tag{39}$$

where the constant, C, is a function of the column geometry and mass transfer, and may also depend upon the liquid–liquid system employed [37]. According to Eq.39, a decrease in droplet size is expected with a decrease in the interfacial tension of systems.

The effect of mass transfer direction on mean drop sizes is shown in Figs. 8, 9 and 10. The presence of a solute tends to lower the interfacial tension between the two immiscible liquids. The drop behavior could be due to Marangoni thin film phenomena. When the mass transfer direction happens from the dispersed to the continuous phase (d to c), the solute concentration in the draining film between the two adjacent drops will be higher than in the surrounding continuous liquid. As for mass transfer in the opposite direction (c to d), the concentration will be correspondingly lower. The gradients of interfacial tension will accelerate drainage and coalescence in the former case and retard drainage and inhibit coalescence in the latter case. Therefore, d to c transfer tends to produce larger drops and c to d transfer is apt to smaller drops.

5.1.1. Comparison of the experimental results with previous correlation and prediction of new correlation

The previous correlations in Table 1 were selected for comparison with the experimental data. The results of the comparison are presented in Fig. 11 and Table 3. It is obvious, from the results that the previous correlations could not accurately predict and fit the measured data. They particularly failed to represent the trends of the mass transfer direction on the Sauter mean drop diameter; they were proposed for only toluene-water system.

The following correlation is derived for the mean drop size in the multi-impeller column extractor based on the operating parameters, physical properties and column geometry. This correlation is derived based on the experimental results of the present work and the data taken from other researchers in Table 1.

$$d_{32} = C_1\left(\frac{N^4 d_R^4 \rho_c}{g\sigma}\right)^{-0.277}\left(\frac{\mu_c^4 g}{\Delta\rho\sigma^3}\right)^{-0.082}\left(1+\frac{V_c}{V_d}\right)^{-0.328}\eta^{C_2}\left(\frac{h_c}{d_R}\right)^{C_3} \quad (40)$$

The effect of mass transfer and column geometry on the Sauter mean drop diameter is shown by constant parameters, C_1, C_2, C_3 in the above equation, respectively. The values of these parameters are presented in Table 4.

A comparison of the prediction of the proposed correlation was tested, as shown in Fig. 12. Also, a comparison of the experimental data of Al-Aswad et al., 1985[38] for RDC Column and other researchers mentioned in Table1 with that predicted by the new correlation, is illustrated in this Figure. The figures shown correlate the predicted values with those experimentally measured ones under different operating conditions and the results with other researchers.

5.2. Drop size distribution

The drop size distributions have a particular form (narrow, wide, few large drops, few small drops) for different extraction columns. Knowledge of the effect of variation in fluid physical properties, column geometry and operating parameters on drop size distribution is crucial if control of the resulting distribution is to be realized.

5.2.1. Effect of operating parameters on drop size distribution

The amount of drop size distribution for three different systems with rotor speed is shown in Fig. 13. The drop size distributions shifted to the left with an increase in agitation, thus evidencing that smaller droplets and more uniform distributions are obtained in more turbulent conditions. This is expected since increasing the agitation speed results in greater average and maximum turbulent energy dissipation per unit mass. This greater turbulence energy results in greater drop breakage rates and/or smaller coalescence rates. The latter is due to the hindering of the colliding drops coalescence by the increased turbulent energy dissipation. In addition, the collision between the organic liquid drop and the internal wall in more turbulent environments leads to the decrease in drop diameter.

The effect of interfacial tension on drop size distributions is shown in Fig.13. The drops produced by n-butanol-water (lower interfacial tension) are smaller and more uniform in size than the ones produced by the other systems.

Figs. 14 and 15 show the drop size distribution for different dispersed and continuous phase velocities. A quasi Gaussian distribution is obtained over the whole range of velocities studied. No significant effect was observed in the drop size distribution with variation in the flow rate of the dispersed or continuous phase. Thus, the drop size distribution is independent of both phase flow rates.

5.2.2. Maximum entropy approach for drop size distribution

The maximum entropy principles were applied to obtain the probability density distributions for drops in the multi-impeller column contactor. The probability density is the ratio of drops number with a certain diameter to the total drops number. In order to compare the experimental drop size distributions with the distribution function expressed by maximum entropy in Eq. (20), it is necessary to determine the Lagrange multipliers (λ). The evaluated parameters for λ_0, λ_1 and λ_2 were correlated as a function of operating variables and physical properties of the systems. The derived correlations are given below:

$$\lambda_0 = 21.07\left(\frac{N^4 d_R^4 \rho_c}{\sigma g}\right)^{-0.117}\left(\frac{\mu_c^4 g}{\Delta\rho\sigma^3}\right)^{0.056} \tag{41}$$

$$\lambda_1 = -109.81\left(\frac{N^4 d_R^4 \rho_c}{\sigma g}\right)^{0.202}\left(\frac{\mu_c^4 g}{\Delta\rho\sigma^3}\right)^{0.099} \tag{42}$$

$$\lambda_2 = 0.0235\left(\frac{N^2 d_R^2}{g}\right)\left(\frac{\rho_c}{\Delta\rho}\right)^{-8.631}\left(\frac{\mu_d}{\mu_c}\right)^{-22.279}\left(\frac{\mu_c g^{0.25}}{\rho_c^{0.25}\sigma^{0.75}}\right)^{-3.132}\left(1+\frac{V_c}{V_d}\right)^{0.979} \tag{43}$$

In the latter equations, N, d_R, ρ_c, μ_c, μ_d, σ, $\Delta\rho$, V_c, V_d and g denote the agitation speed, rotor diameter, density of the continuous phase, viscosity of the continuous phase, viscosity of the dispersed phase, interfacial tension, density difference between continuous and dispersed phases, continuous velocity, dispersed velocity and gravity acceleration, respectively. It is observed from the above equations that drop size distribution profiles are significantly affected by rotational speed and surface tension.

Each experimental drop size histogram was compared with probability density function from maximum entropy approach and the average absolute relative errors (*AARE*) were calculated by the following equation:

$$AARE = \frac{1}{n}\sum_{i=1}^{n}\frac{\left|P_i(d)(exp) - P_i(d)(theo)\right|}{P_i(d)(exp)} \qquad (44)$$

where n denotes the number of data points, and $P_i(d)(exp)$ and $P_i(d)(theo)$ denote the experimental and maximum entropy estimation number densities of the drops, respectively.

The values of *AARE* are shown in Table 5. It is observed that the use of maximum entropy principles was found to results in good agreement with the experimental data.

5.2.3. Compare maximum entropy approach with PBM and CFD Simulation

In order to test the validity of the maximum entropy method, the results from this method are compared with the experimental data and the results from PBM and CFD simulation. The comparison of the results is shown in Fig. 16. It is observed that the experimental data are close to the predicted results from the two methods. It is found that the results are predicted with 10.5% and 6.5% relative error with the maximum entropy method and PBM and CFD simulation, respectively. The differences between the experimental data and the simulated results with PBM and CFD increase as the level of agitation increase. The differences are attributed to inadequacies of the breakage and exit frequencies, and reflect the lack of experimental information on the continuous phase hydrodynamics and the velocity of drops in the multi-impeller column. The results obtained with the maximum entropy method are independent from the information for breakage and coalescence process. In addition, the solution program time for prediction with this method is very low in comparison with PBM and

CFD simulation. Therefore, the maximum entropy method will be useful for prediction of drop size distribution in liquid-liquid extraction columns without the requirement for the solutions of population balance equations.

6. Conclusion

Drop size distribution and Sauter mean drop size in the multi-impeller column extractor were investigated in this research work. The drop size could be decreased with increasing agitation speed and decreasing dispersed phase flow rate, but the continuous phase flow rate does not have a significant effect. Also, it is observed that the direction of mass transfer influenced in the Sauter mean drop diameter. The maximum entropy method has been used to derive the most probable drop size distribution in this column. The drop size distribution predicted from the statistical approach are compared with experimental data and the computational fluid dynamics and droplet population balance modeling to evaluate the maximum entropy approach developed in this study. The drop size distribution has been correlated to the operating parameters and physical properties for the three systems in the frame of the maximum entropy method. It is observed that maximum entropy method reliably estimates the probability drop size distribution in multi-impeller column extractor and would be useful for liquid-liquid extraction processes where the drop breakup is stochastic in nature.

Nomenclature

a	coalescence rate (1/s)
$AARE$	average absolute relative error (-)
C_d	drag coefficient (-)
C_{II}	constant parameter in Eq.2 (-)
C_{Ψ}	constant parameter in Eq.2 (-)
C_{Ω}	constant parameter in Eq.2 (-)

d_{30}	volume drop diameter (m^3)
d_{32}	Sauter mean drop diameter (m)
D_c	column diameter (m)
D_i	droplet diameter (m)
d_R	rotor diameter (m)
e	power dissipated per unit mass ($m^2.s^3$)
F_{in}	force interaction (N)
$F_{c,d}$	drag force (N)
g	acceleration due to gravity (m/s^2)
g_b	Breakage frequency (1/s)
H	effective height of the column (m)
h_c	compartment height (m)
h	Collision frequency (1/s)
k	Kinetic energy (m^2/s^2)
m	mass (kg)
m°	mass flow rate per surface area ($kg/(m^2.s)$)
N	rotor speed (1/s)
n_i	number of droplets of mean diameter d_i (-)
P	probability of number density (-)
Q	flow rate of the continuous or dispersed phase (m^3/s)
S	Shannon entropy (-)
u	Phase velocity (m/s)
V	superficial velocity (m/s)
V_i	impeller tip velocity (m/s)
V_k	characteristic velocity (m/s)

Greek

σ	interfacial tension (N/m)
α	Volume fraction (-)
β	Probability density function (-)
δ	Coalescence efficiency (1/s)

$\Delta\rho$	density difference between phases (kg/m^3)
ε	Energy dissipation (m^2/s^3)
η	cross sectional area (-)
λ	Lagrange multipliers of probability maximum entropy function
μ	viscosity (Pa.s)
ρ	density (kg/m^3)
ρ_m	density of dispersion (kg/m^3)
τ	Stress strain tensor (N/m)
φ	dispersed phase holdup (-)

Subscripts

c	continuous phase
d	dispersed phase

References

1. V. S. Kislik, *Solvent Extraction: Classical and Novel Approaches*, Elsevier, New York, 2012.
2. J. C. Godfrey and M. J. Slater, *Liquid-Liquid Extraction Equipment*, Wiley, New York, 1994.
3. J. H. Rushton, S. Nagata and T. B. Rooney, *AIChE J.*, 1964, **10**, 298-302.
4. L. Steiner, E. V. Fisher and S. Hartland, *AIChE Symp. Ser.*, 1984, **80**, 130-138.
5. N. S. Oliveira, D. M. Silva, M. P. C. Gondim and M. B. Mansur, *Braz. J. Chem. Eng.*, 2008, **25**, 729-740.
6. J. Rydberg, C. Musikas and G. R. Choppin, *Solvent Extraction Principles and Practice*, CRC Press, New York, 2004.
7. I. Komasawa and J. Ingham, *Chem. Eng. Sci.*, 1978, **33**, 479-485.
8. C. Tsouris, R. Ferreira and L. L. Tavlarides, *Can. J. Chem. Eng.*, 1990, **68**, 913-923.

9. S. H. Zhang, S. C. Yu, Y. C. Zhou and Y. F. Su, *Can. J. Chem. Eng.*, 2009, **63**, 212-226.
10. W. L. Chen, L. M. Zhong, L. Chen and W. Weiyang, *Chem. Eng. Sci.*, 2013, **102**, 622-631.
11. E. Moreira, L. M. Pimenta, L. LCarneiro, R. C. L. Faria, M. B. Mansur and J. P. Ribiero, *Chem. Eng. Commun.*, 2007, **192**, 1017-1035.
12. L. S. Tung and R. H. Luecke, *Ind. Eng. Chem. Process Des. Dev.*, 1986, **25**, 664-673.
13. L. M. Rincon-Rubio, A. Kumar and S. Hartland, *Chem. Eng. Res. Des.*, 1994, **72**, 493-502.
14. A. S. Ismail, *Can. J. Chem. Eng.*, 2002, **82**, 1037-1043.
15. T. Steinmetz and H. J. Bart, *Chem. Eng. Technol.*, 2009, **32**, 693-709.
16. M. Attarakih, M. Abu-Khader and H. J. Bart, *Chem. Eng. Sci.*, 2013, **91**, 180-196.
17. J. M. Bujalski, W. Yang, J. Nikolov, C. B. Solnordal and M. P. Schwarz, *Chem. Eng. Sci.*, 2006, **61**, 2930-2938.
18. R. L. Yadav and A. W. Patwardhan, *Chem. Eng. Res. Des.* , 2009, **87**, 25-35.
19. G. U. Din, I. R. Chughtai, M. H. Inayat, I. H. Khan and N. K. Qazi, *Sep. Purif. Technol.*, 2010, **73**, 302-309.
20. F. Onink, C. Drumm, G. W. Meindersma, H. J. Bart and A. B. d. Haan, *Chem. Eng. J.*, 2010, **160**, 511-521.
21. A. Hasseinea and H. J. Bart, *Appl. Math. Model.*, 2015, **39**, 1975-1984.
22. F. Buchbender, F. Onink, W. Meindersma, A. d. Haan and A. Pfenning, *Chem. Eng. Sci.*, 2012, **82**, 167-176.
23. E. Babinsky and P. E. Sojka, *Prog. Energ. Combust.*, 2002, **28**, 303-329.
24. M. Tembely, C. Lecot and A. Soucemarianadin, *App. Thermal Eng.*, 2011, **31**, 656-667.

25. A. Shannon, *Bell Syst. Tech. J.*, 1948, **27**, 379-423.

26. E. T. Jaynes, *Phys. Rev*, 1957, **106**, 620-630.

27. M. Tribus and N. Princeton, *Thermostatics and Thermodynamics*, Van Nostrand, New York, 1961.

28. C. Sobrino, J.A.Almendros-Ibáñez, D.Santana, C.Vázquez and M.deVeg, *Chem. Eng. Sci*, 2009, **64**, 2307-2319.

29. D. P. Jones and A. P. Watkins, *J. Comput. phys.*, 2012, **231**, 676-692.

30. S. Sankaran and N. Zabaras, *Acta Materialia*, 2007, **55**, 2279-2290.

31. L. Schiller and Z. Naumann, *Z. Ver. Deutsch. Ing.*, 1935, 77-318.

32. F. Kerdouss, A. Bannari and P. Proulx, *Chem. Eng. Sci.*, 2006, **61**, 3313-3322.

33. C. A. Coulaloglou and L. L. Tavlarides, *Chem. Eng. Sci.*, 1977, **32**, 1289-1297.

34. K. J. Valentas, O. Bilous and N. R. Amundson, *Ind. Eng. Chem. Fund.*, 1966, **5**, 271-279.

35. T. Míšek, R. Berger and J. Schroter, *Standard test systems for liquid extraction studies*, EFCE Publ. Ser., 1985.

36. M. Torab-Mostaedi, A. Ghaemi and M. Asadollahzadeh, *Can. J. Chem. Eng.*, 2012, **90**, 1569-1577.

37. A. Kumar and S. Hartland, *Ind. Eng. Chem. Res.* , 1996, **35**, 2682-2695.

38. K. K. AL-Aswad, C. J. Mumford and G. V. Jeffreys, *AIChE J.* , 1985, **31**, 1488-1497.

39. A. Kumar and S. Hartland, *Can. J. Chem. Eng.*, 1986, **64**, 915-924.

40. D. R. Arnold, C. J. Mumford and G. V. Jeffreys, in International Solvent Extraction Conference ISEC'74, Lyon, September, 1974.

41. A. M. I. Al-Rahawi, *Chem. Eng. Technol.*, 2007, **30**, 184-192.

42. A. Hemmati, M. Torab-Mostaedi, M. Shirvani and A. Ghaemi, *Chem. Eng. Res. Des.*, 2015, **96**, 54-62.

Figure Captions:

Fig.1. Definition of relevant parameters in droplet size distribution.

Fig.2. Two fluid CFD and PBM Model

Fig.3. Graphical representation of the different expressions in the drop population-balance equation

Fig.4. Schematic flow diagram of multi-impeller column extractor.

Fig.5. The variation of the Sauter mean drop diameter with rotor speed (V_c= V_d= 0.66 mm/s).

Fig.6. The variation of the Sauter mean drop diameter with the dispersed phase velocity for the binary systems of toluene- water (T/W) , n-butyl acetate- water (B/W) and n-butanol-water (Bu/W) (V_c= 0.66 mm/s).

Fig.7. The variation of the Sauter mean drop diameter with the continuous phase flow rate for the binary systems of toluene- water (T/W) , n-butyl acetate- water (B/W) and n-butanol-water (Bu/W) (V_d= 0.66 mm/s).

Fig.8. The photo of drops for three systems without mass transfer condition (a) Toluene -water (b) n-butyl acetate-water, (c) n-butanol-water and Toluene-acetone-water with mass transfer (d) d to c transfer and (e) c to d transfer (V_c= V_d=0.66 mm/s, N=140 rpm).

Fig.9. Effect of mass transfer direction on the Sauter mean drop diameter for toluene-acetone-water (a) variation with V_c (V_d=0.66 mm/s), (b) variation with V_d (V_c=0.66 mm/s), (c) variation with rotor speed (V_d= V_c=0.66 mm/s)

Fig.10. Effect of mass transfer direction on the Sauter mean drop diameter for n-butyl acetate-acetone-water (a) variation with V_c (V_d=0.66 mm/s), (b) variation with V_d (V_c=0.66 mm/s), (c) variation with rotor speed (V_d= V_c=0.66 mm/s)

Fig.11. Comparison of the values calculated previous correlation in Table 1 with experimental results.

Fig.12. Comparison between experimental data and the evaluated values using Eq. 40 for (a) no mass transfer condition and (b) two directions of mass transfer conditions.

Fig.13. Effect of rotor speed on the drop size distribution (m°_{c}= 0.665 kg/(m^2.s), m°_{d}= 0.577 kg/(m^2.s)).

Fig.14. Effect of dispersed phase flow rate on the drop size distribution at the same rotor speed for the binary systems of (a) toluene- water (T/W), (b) n-butyl acetate- water (B/W) and (c) n-butanol-water (Bu/W) (N=140 rpm, m°_{c}= 0.665 kg/(m^2.s)).

Fig.15. Effect of continuous phase flow rate on the drop size distribution at the same rotor speed for the binary systems of (a) toluene- water (T/W), (b) n-butyl acetate- water (B/W) and (c) n-butanol-water (Bu/W) (N=140 rpm, m°_{c} = 0.577 kg/(m^2.s)).

Fig.16. Comparison of maximum entropy distribution functions with a broad drop size distribution for (a) toluene-water and (b) n-butyl acetate-water (N=140 rpm, m°_{c}= 0.665 kg/(m^2.s), m°_{d}= 0.577 kg/(m^2.s)).

Tables list:

Table 1. Unified correlations for prediction of the drop size in mechanically agitated columns.

Table 2. Physical properties of systems studied a 20ºC [35].

Table 3. The values of *AARE* in the predicted values of Sauter mean drop diameter obtained by previous correlations.

Table 4. The constants and *AARE* values of Eq. 40.

Table. 5. The obtained average absolute relative errors for estimation of Lagrange multipliers in maximum entropy function.

Table 1. Unified correlations for prediction of the drop size in mechanically agitated columns.

Equation		Column	Reference
For $Re \leq 50000$ $\frac{d_{32}}{D_c} = 0.18\left(\frac{N D_c^{2} \rho_c}{\mu_c}\right)^{-1.12}\left(\frac{\mu_c}{\sqrt{\sigma \rho_c D_c}}\right)^{-1.38}\left(\frac{\Delta\rho}{\rho_c}\right)^{-0.24}\left(\frac{D_c^{2} \rho_c g}{\sigma}\right)^{-0.05}\left(\frac{h}{d_R}\right)^{0.42}$	(1)	Rotating disc column	Kumar and Hartland, 1986 [39]
$\frac{d_{32}}{H} = \frac{C_{\psi} e^{n}}{\frac{1}{C_{\Omega}\left(\frac{\sigma}{\Delta\rho g H^{2}}\right)^{1/2}} + \frac{1}{C_{II}\left[\left(\frac{\varepsilon}{g}\right)\left(\frac{\rho_c}{g\sigma}\right)^{1/4}\right]^{n_1}\left[H\left(\frac{\rho_c g}{\sigma}\right)^{1/2}\right]^{n_2}}}$	(2)	Rotating disc column Asymmetric rotating disc column Kühni Column Wirtz Column Pulsed column Karr Column	Kumar and Hartland, 1996 [37]
$\frac{d_{32}}{D_i} = 2.44\left(\frac{h}{H}\right)^{-0.06}\left(\frac{V_i^{2} D_i \rho_m}{\sigma_i}\right)^{-0.63}\left(\frac{V_k}{V_i}\right)^{0.18}$	(3)	Multi-impeller column extractor	Arnold et al., 1974 [40]
$\frac{d_{32}}{d_R} = 90.7\left(\frac{h}{H}\right)^{-0.13}\left(\frac{V_i^{2} d_R \rho_m}{\sigma_i}\right)^{-0.39}\left(\frac{V_k}{V_i}\right)^{0.40}\varphi^{-0.31}$	(4)	Multi-impeller column extractor	Tsouris et al., 1990 [8]
$d_{32} = 0.705\left(\frac{\sigma}{g\Delta\rho}\right)^{0.5}\frac{d_R^{0.8}}{N^{0.185}}\frac{\left(\frac{Q_c}{Q_d}\right)^{0.15}}{\left(Q_c + Q_d\right)^{0.1}}$	(5)	Rotating disc column	Al-Rahawi, 2007 [41]
$d_{32} = 10\left(\frac{N^{4} d_R^{4} \rho_c}{\sigma g}\right)^{-0.296}\left(\frac{\mu_c^{4} g}{\Delta\rho\sigma^{3}}\right)^{-0.087}\left(1 + \frac{V_c}{V_d}\right)^{-0.402}$	(6)	Perforated rotating disc Column	Hemmati et al., 2015 [42]

Table 2. Physical properties of systems studied a 20ºC [35].

Physical property	Toluene-water	n-Butyl acetate-water	n-Butanol-water
ρ_c [kg/m^3]	998.2	997.6	985.6
ρ_d [kg/m^3]	865.2	880.9	846.0
μ_c [mPa.s]	0.963	1.027	1.426
μ_d [mPa.s]	0.854	0.734	3.364
σ [mN/m]	36	14.1	1.75

Table 3. The values of *AARE* in the predicted values of Sauter mean drop diameter obtained by previous correlations

Equation	Averaged absolute values of the relative error (*AARE*)
Rotating disc column, Eq.1	38.42%
Rotating disc column, Eq.2	51.29%
Kühni column, Eq.2	43.90%
Multi-impeller column extractor, Eq.3	36.57%
Multi-impeller column extractor, Eq.4	37.94%
Rotating disc column, Eq.5	69.99%
Perforated rotating disc column, Eq.6	26.35%

Table 4. The constants and *AARE* values of Eq. 40.

Mass transfer condition	C_1	C_2	C_3	*AARE*%
no mass transfer	3.36×10^{-4}	-0.434	-0.711	7.48
continuous to dispersed transfer (c→d)	1.96×10^{-4}	-0.806	-0.820	7.26
dispersed to continuous transfer (d→c)	2.78×10^{-4}	-0.548	-0.689	10.71

Table 5. The obtained average absolute relative errors for estimation of Lagrange multipliers in maximum entropy function.

Parameter of the distribution	*AARE* (%)
λ_0	8.86
λ_1	9.27
λ_2	10.67

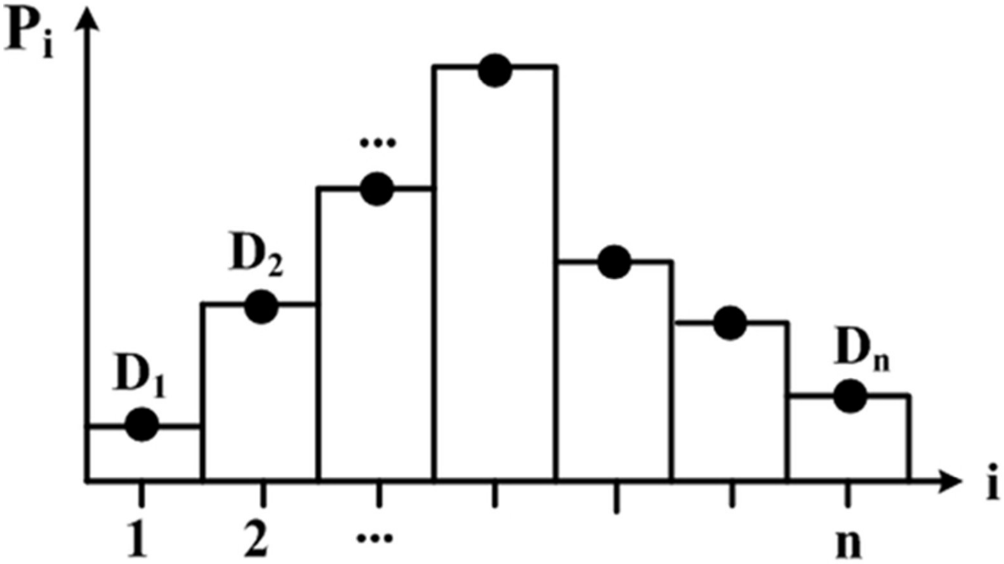

Fig.1. Definition of relevant parameters in droplet size distribution.
49x29mm (300 x 300 DPI)

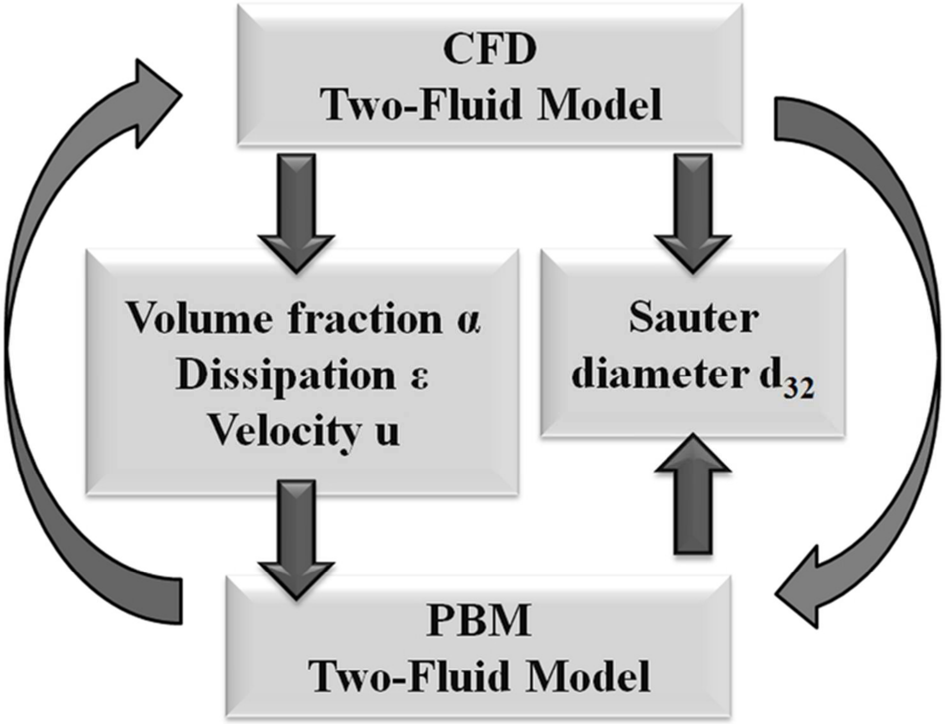

Fig.2. Two fluid CFD and PBM Model
64x50mm (300 x 300 DPI)

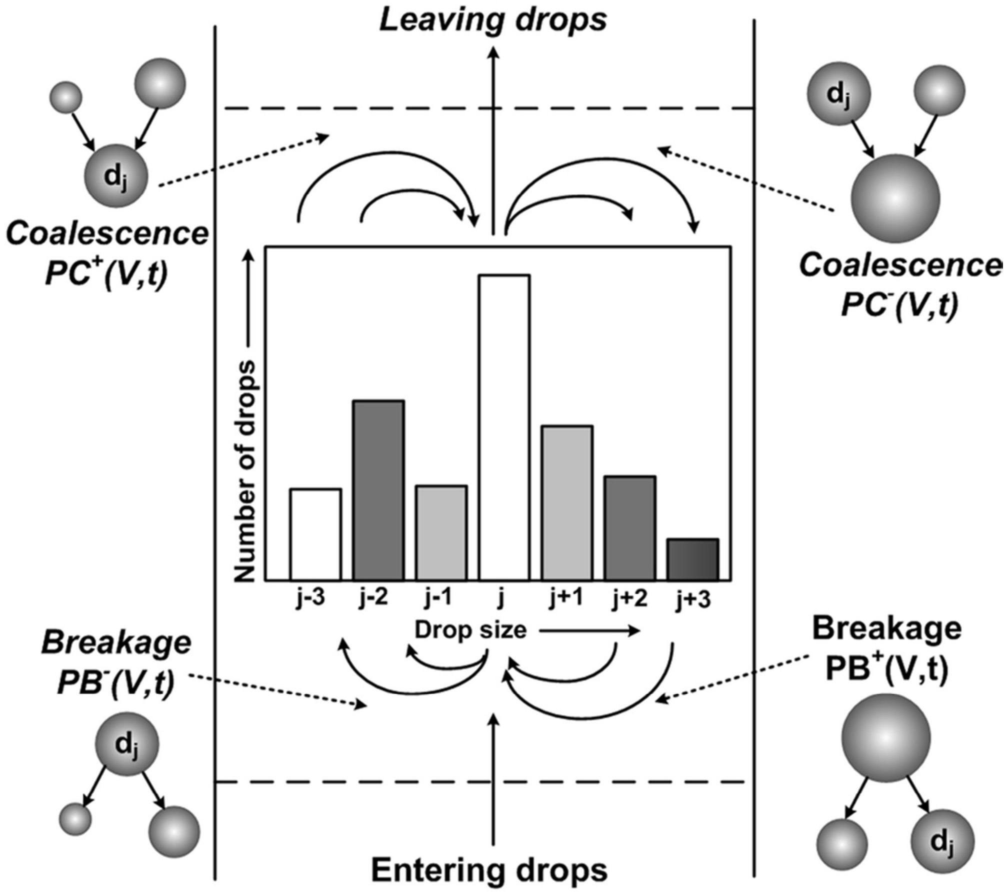

Fig.3. Graphical representation of the different expressions in the drop population-balance equation
74x66mm (300 x 300 DPI)

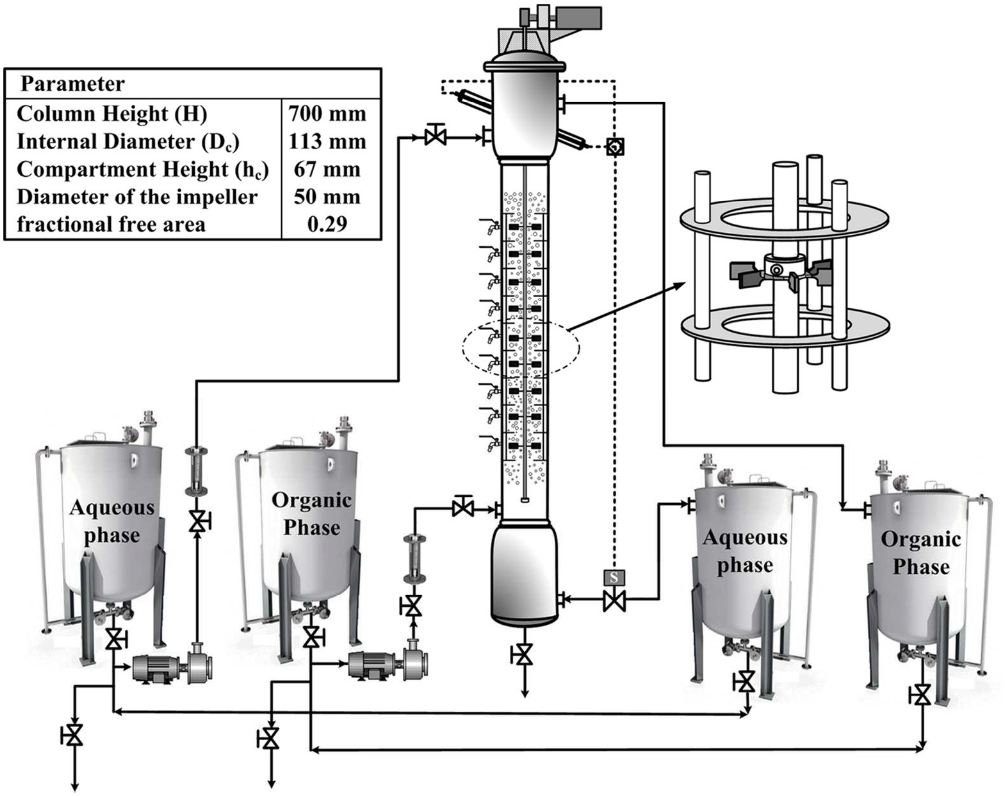

Parameter	
Column Height (H)	700 mm
Internal Diameter (D_c)	113 mm
Compartment Height (h_c)	67 mm
Diameter of the impeller	50 mm
fractional free area	0.29

Fig.4. Schematic flow diagram of multi-impeller column extractor.
134x106mm (300 x 300 DPI)

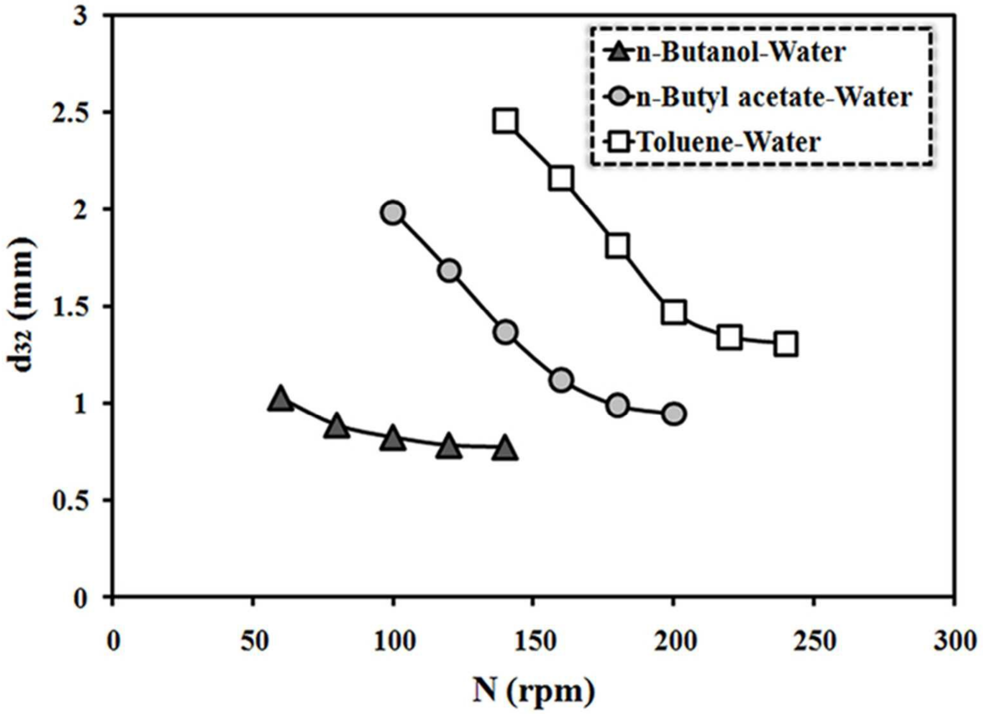

Fig.5. The variation of the Sauter mean drop diameter with rotor speed (Vc= Vd= 0.66 mm/s).
60x44mm (300 x 300 DPI)

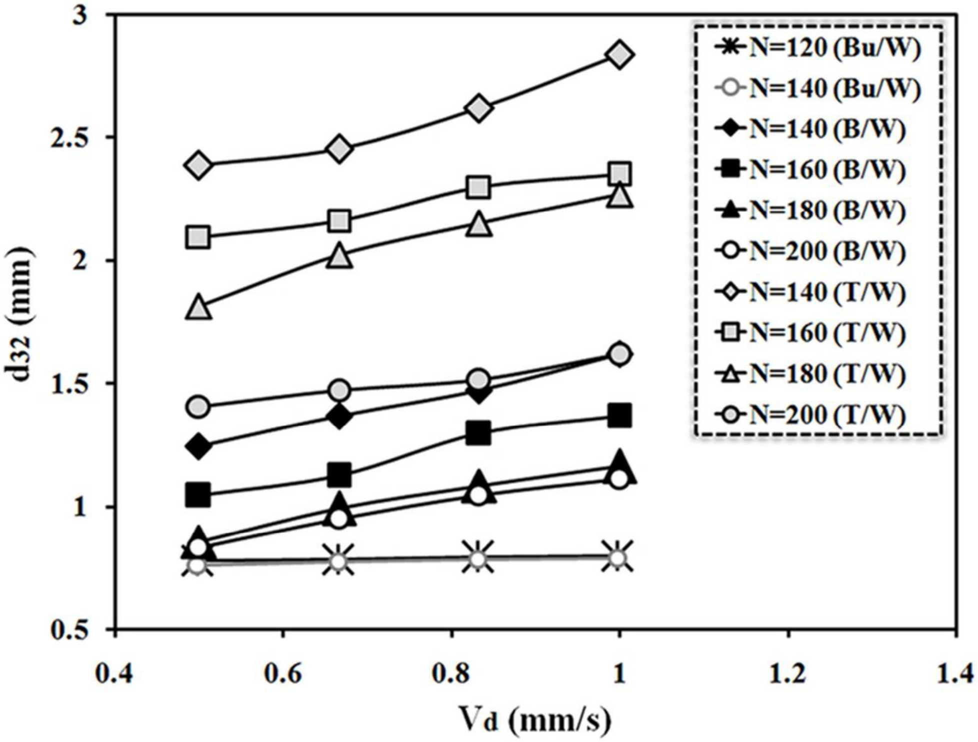

Fig.6. The variation of the Sauter mean drop diameter with the dispersed phase velocity for the binary systems of toluene- water (T/W) , n-butyl acetate- water (B/W) and n-butanol-water (Bu/W) (Vc= 0.66 mm/s).
62x46mm (300 x 300 DPI)

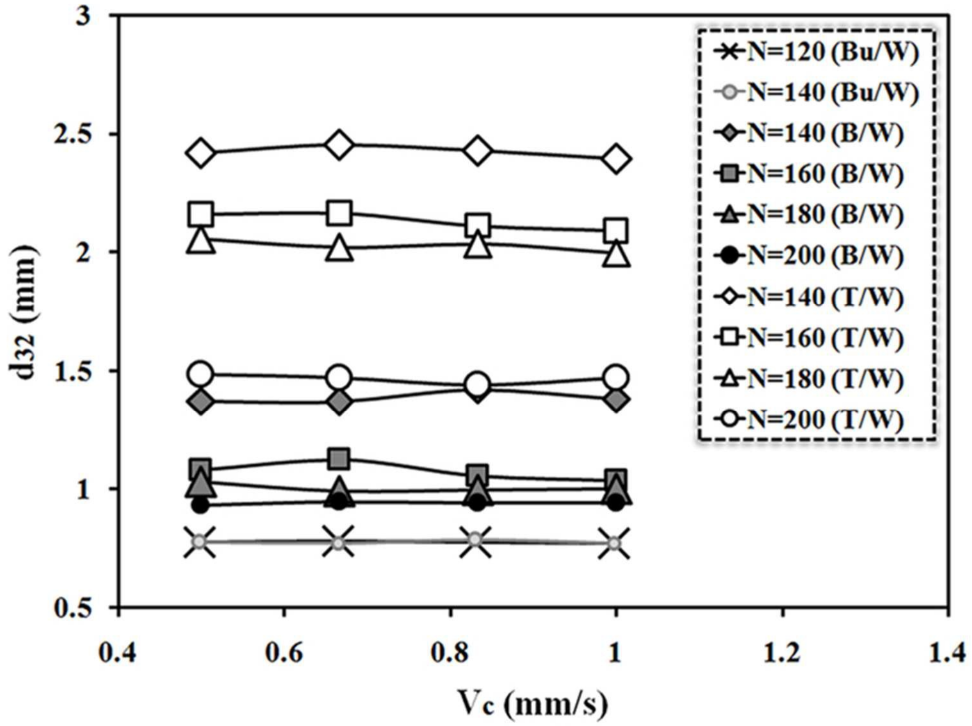

Fig.7. The variation of the Sauter mean drop diameter with the continuous phase flow rate for the binary systems of toluene- water (T/W) , n-butyl acetate- water (B/W) and n-butanol-water (Bu/W) (Vd= 0.66 mm/s).
62x46mm (300 x 300 DPI)

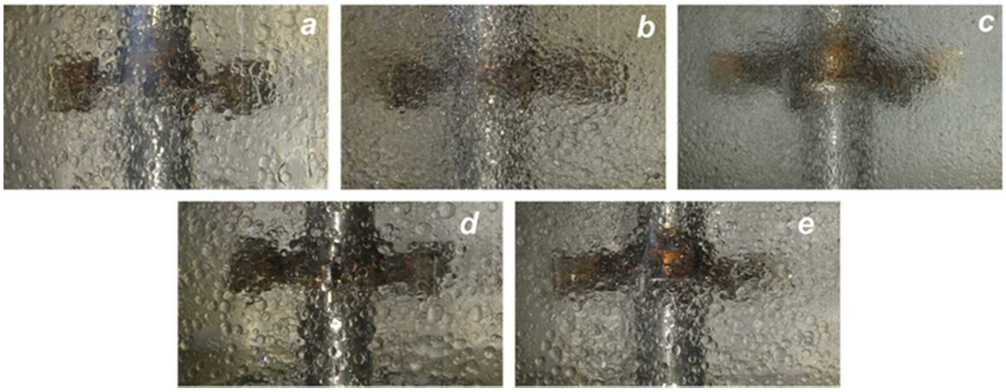

Fig.8. The photo of drops for three systems without mass transfer condition (a) Toluene -water (b) n-butyl acetate-water, (c) n-butanol-water and Toluene-acetone-water with mass transfer (d) d to c transfer and (e) c to d transfer (Vc= Vd=0.66 mm/s, N=140 rpm).
66x25mm (300 x 300 DPI)

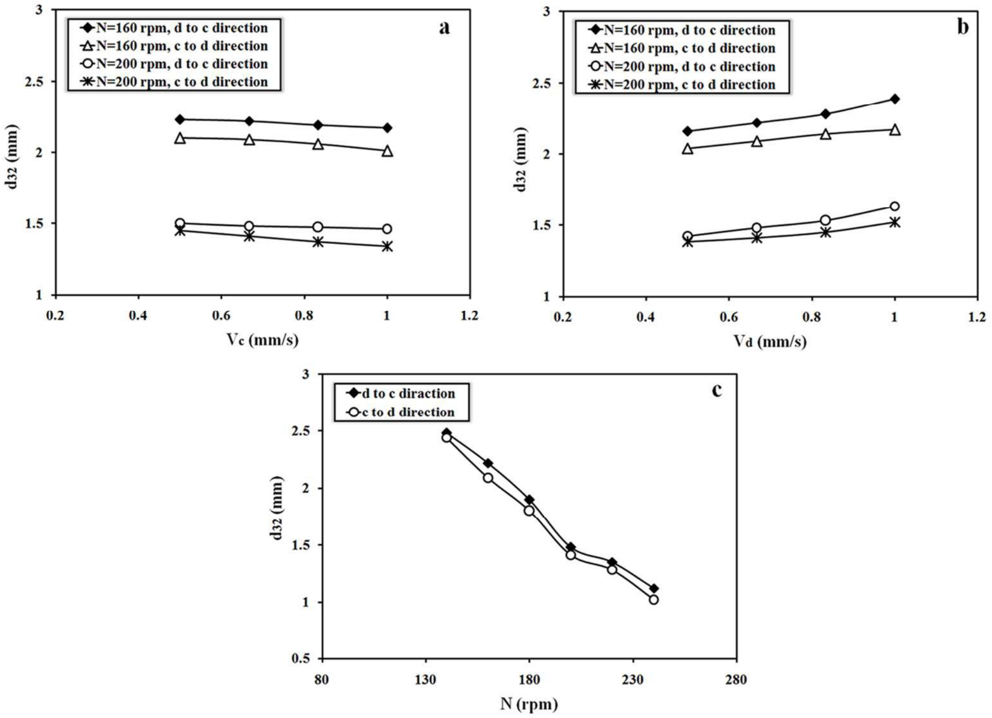

Fig.9. Effect of mass transfer direction on the Sauter mean drop diameter for toluene-acetone-water (a) variation with Vc (Vd=0.66 mm/s), (b) variation with Vd (Vc=0.66 mm/s), (c) variation with rotor speed (Vd= Vc=0.66 mm/s)
123x89mm (300 x 300 DPI)

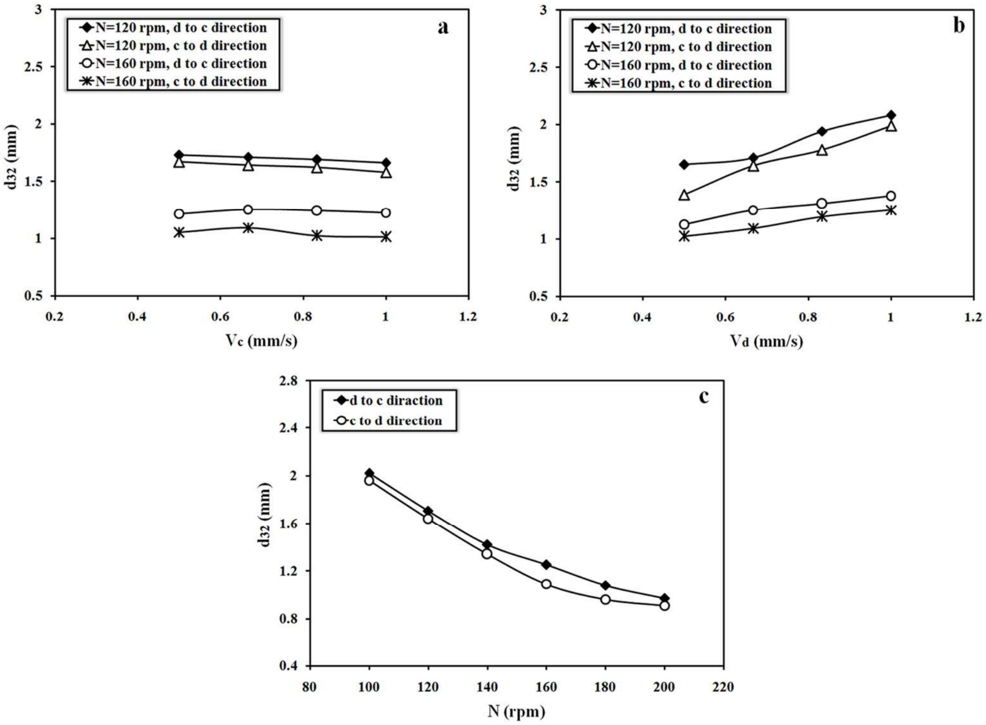

Fig.10. Effect of mass transfer direction on the Sauter mean drop diameter for n-butyl acetate-acetone-water (a) variation with Vc (Vd=0.66 mm/s), (b) variation with Vd (Vc=0.66 mm/s), (c) variation with rotor speed (Vd= Vc=0.66 mm/s)
125x92mm (300 x 300 DPI)

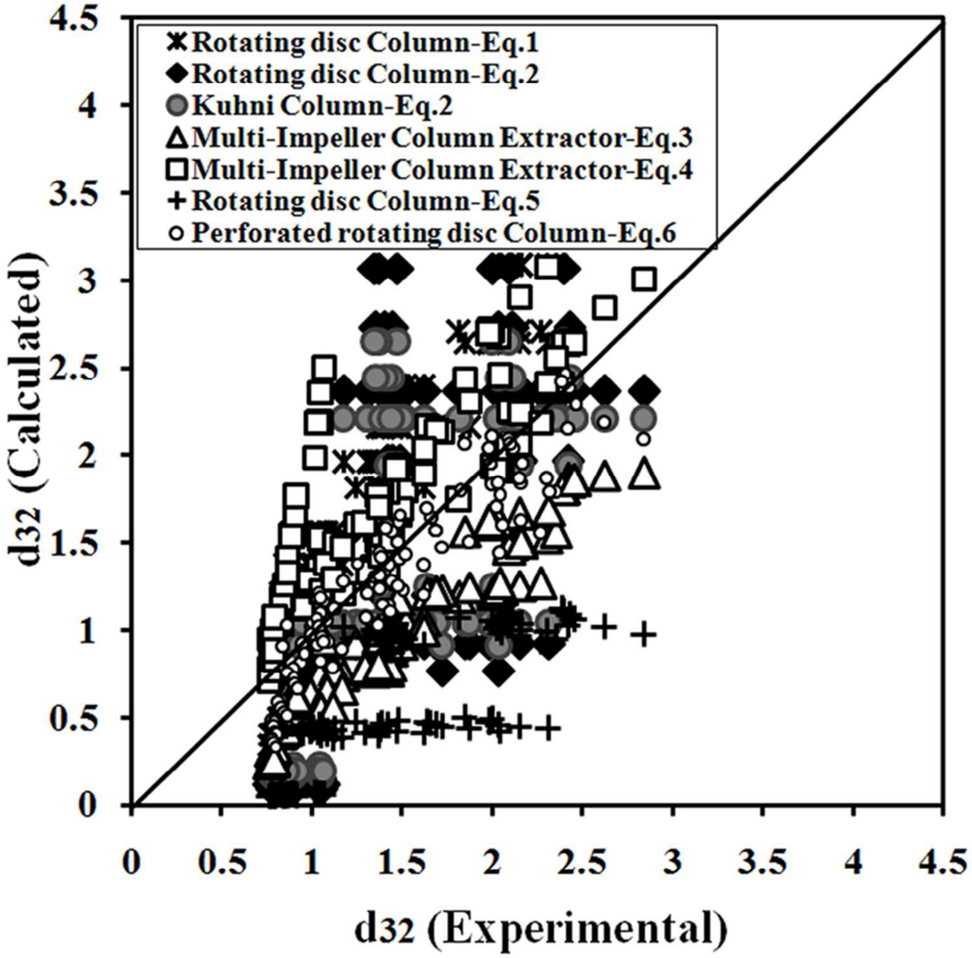

Fig.11. Comparison of the values calculated previous correlation in Table 1 with experimental results.
81x79mm (300 x 300 DPI)

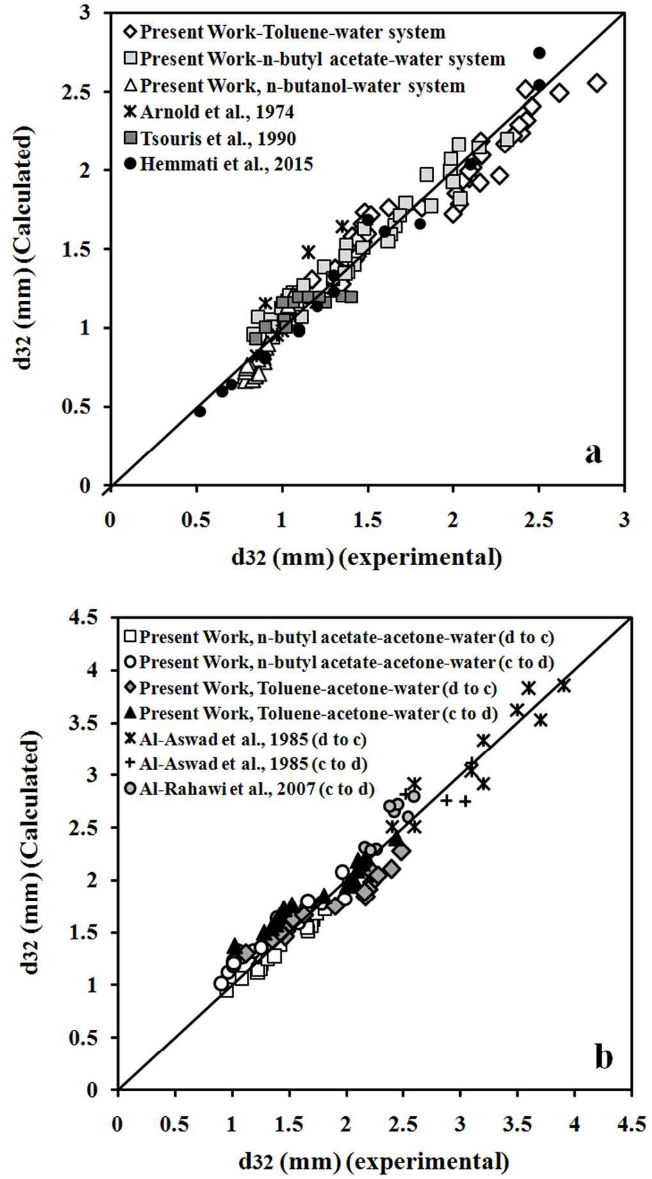

Fig.12. Comparison between experimental data and the evaluated values using Eq. 40 for (a) no mass transfer condition and (b) two directions of mass transfer conditions.
149x270mm (300 x 300 DPI)

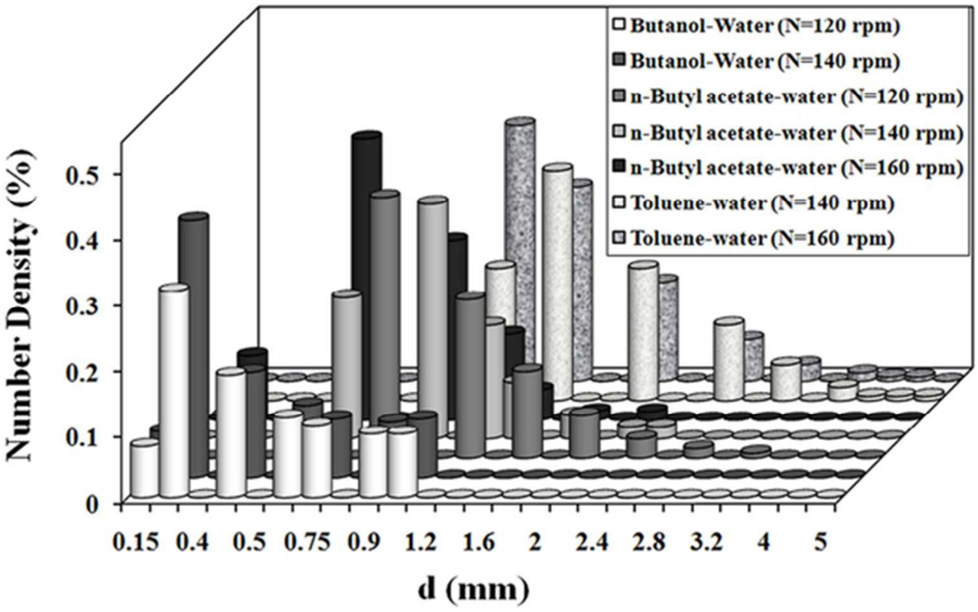

Fig.13. Effect of rotor speed on the drop size distribution (m˚c= 0.665 kg/(m2.s), m˚d= 0.577 kg/(m2.s)).
53x33mm (300 x 300 DPI)

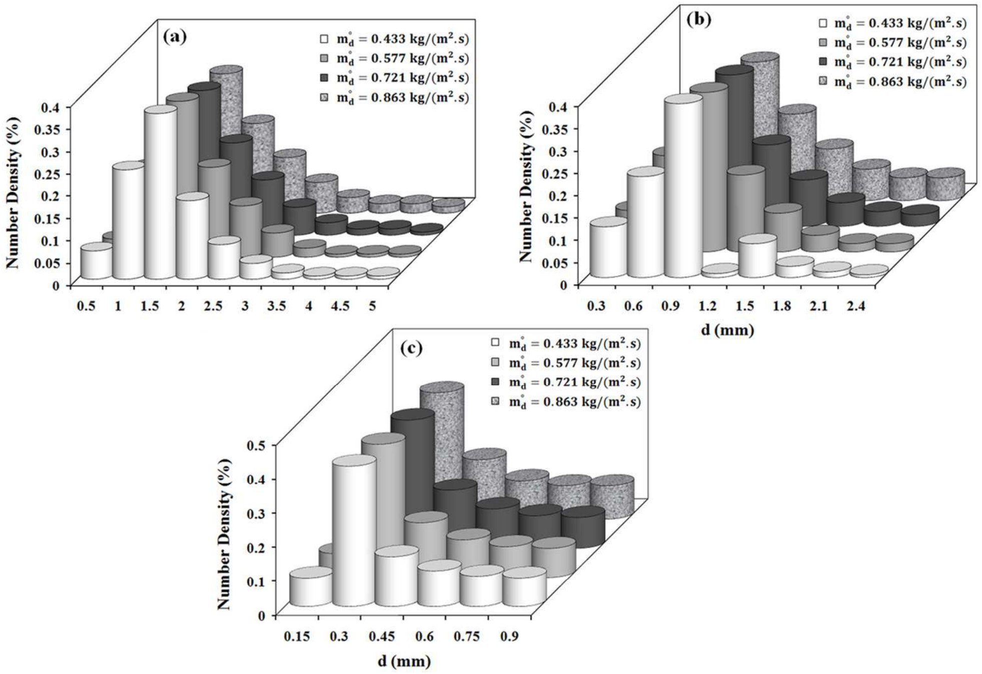

Fig.14. Effect of dispersed phase flow rate on the drop size distribution at the same rotor speed for the binary systems of (a) toluene- water (T/W), (b) n-butyl acetate- water (B/W) and (c) n-butanol-water (Bu/W) (N=140 rpm, m˚c= 0.665 kg/(m2.s)).
116x79mm (300 x 300 DPI)

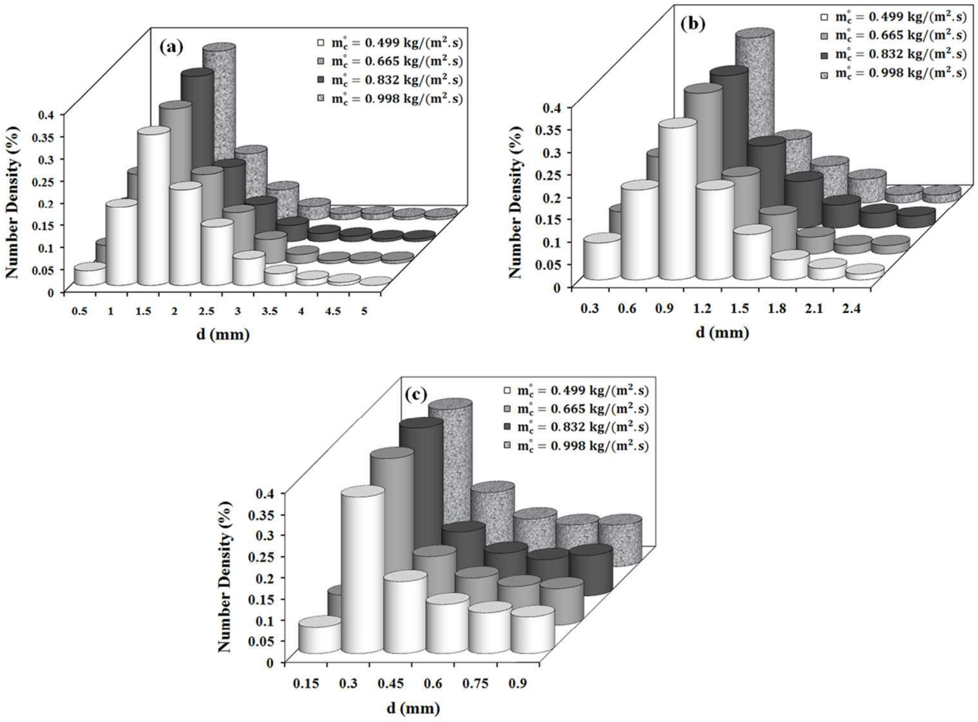

Fig.15. Effect of continuous phase flow rate on the drop size distribution at the same rotor speed for the binary systems of (a) toluene- water (T/W), (b) n-butyl acetate- water (B/W) and (c) n-butanol-water (Bu/W) (N=140 rpm, m˚c = 0.577 kg/(m2.s)).
125x92mm (300 x 300 DPI)

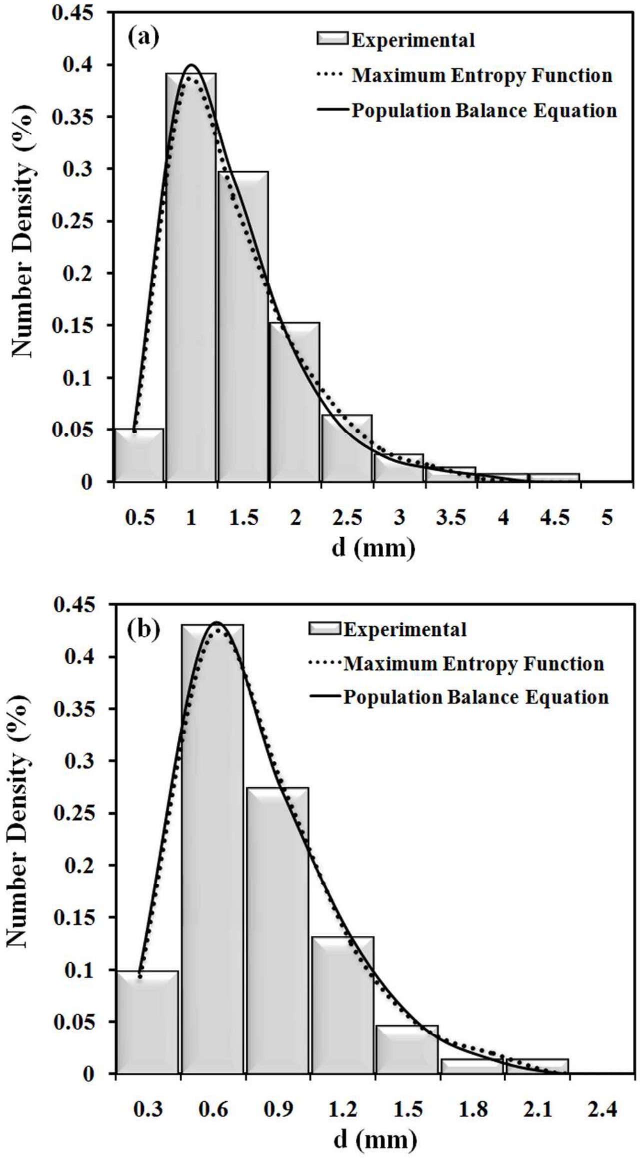

Fig.16. Comparison of maximum entropy distribution functions with a broad drop size distribution for (a) toluene-water and (b) n-butyl acetate-water (N=140 rpm, m˚c= 0.665 kg/(m2.s), m˚d= 0.577 kg/(m2.s)).
148x266mm (300 x 300 DPI)

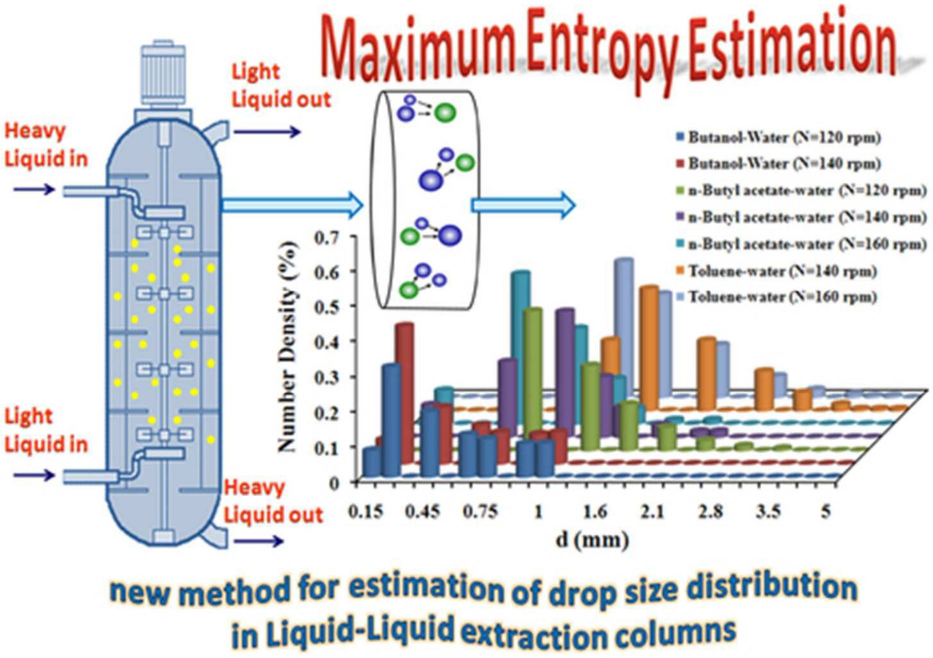

new method for estimation of drop size distribution in Liquid-Liquid extraction columns

39x30mm (300 x 300 DPI)